

# Simulation of Single-Particle Displacement Damage in Silicon—Part III: First Principle Characterization of Defect Properties

Antoine Jay, *Member, IEEE*, Anne Hémercyck, Nicolas Richard<sup>1</sup>, *Member, IEEE*, Layla Martin-Samos, Mélanie Raine<sup>2</sup>, *Member, IEEE*, Alexandre Le Roch, Normand Mousseau, Vincent Goiffon<sup>3</sup>, *Member, IEEE*, Philippe Paillet, *Senior Member, IEEE*, Marc Gaillardin<sup>4</sup>, *Member, IEEE*, and Pierre Magnan, *Member, IEEE*

**Abstract**—A first principle study of the defects generated by displacement cascades in silicon is performed. This paper is particularly focused on two defect configurations; the divacancy and the tri-interstitial, both identified in previous molecular dynamics and kinetic activation relaxation technique simulations. By combining structural, energy and migration properties evaluated within the framework of the standard density functional theory and electronic properties calculated within the  $G_0W_0$  approximation, a reconstruction of the corresponding thermally activated electrical signal generated by each defect is obtained. Their contribution to dark current (DC) and DC random telegraph signal measured in image sensors is then discussed.

**Index Terms**—Dark current (DC), defects, density function theory (DFT), displacement damage (DD), first principle (FP) calculations, GW approximation, kinetic activation relaxation technique (k-ART), nudged elastic band, random telegraph signal (RTS), silicon.

## I. INTRODUCTION

THE need for fundamental understanding of the damaged structures generated at the atomic scale by displacement damage (DD) is a major challenge for the community of radiation effects on micro- and optoelectronics (see [1]). To tackle this question, a novel simulation approach has been developed (see [1], [2]) based on the one proposed in [3]. It combines several simulation steps using different methods linked one to another as shown in Fig. 1: Monte Carlo (MC) particle–matter interaction simulation, molecular

dynamics (MD), kinetic MC (KMC), and first principle (FP) calculations (also called *ab initio* calculations). Results coming from the first, second, and third steps are presented in [1] and [2]. As detailed in [1], the main advantages of this methodology are the following: simulations start from realistic primary knock-on atom (PKA) energies; large statistics of possible PKA directions are simulated, thus resulting in a statistically meaningful library of generated defect configurations; the electronic stopping power is taken into account; and simulation times on the order of 1 s are reached, which gives access to direct comparison with experimental data. This last crucial point has been obtained by using a KMC method called the kinetic activation relaxation technique (k-ART) [2]. This method, by overtaking the timescale limit of classical MD simulations, offers the possibility of relaxing a large library of defects and defect clusters over 1 s after the initial interaction as demonstrated in [2]. The access to this long timescale has enabled to draw some first important conclusions regarding the origin of the radiation-induced dark current (DC) and DC random telegraph signal (DC-RTS) measured in image sensors, as discussed in [2].

- After 1 s of annealing, clusters are mainly constituted of small defect centers, such as divacancy, trivacancy, quadri-vacancy, and tri-interstitial and quadri-interstitial (2–4V and 3–4I, respectively). The absence of the point defects 1V, 1I, and defect center 2I after annealing is due to their small diffusion barriers that allow them to move until their agglomeration or recombination. The quasi-total annealing of large clusters that recover their crystalline form is due to the recombination of Frenkel pairs.
- DC-RTS phenomena seem to be linked to flickering configurations of the same defect center, i.e., different configurations that alternate in time due to the thermal excitation and the low-energy barriers between them. They are surrounded by larger energy barriers that trap the defect center in a small number of configurations.
- The cluster size distribution presents an exponential shape similar to the shape of DC distributions measured experimentally in image sensors [2].

Manuscript received October 27, 2017; revised December 10, 2017; accepted December 11, 2017. Date of publication January 8, 2018; date of current version February 13, 2018. This work was supported by HPC resources from GENCI-CCRT under Grant A0010907474 and from CALMIP under Grant P1555.

A. Jay, A. Le Roch, V. Goiffon, and P. Magnan are with ISAE, Université de Toulouse, 31055 Toulouse, France (e-mail: antoine.jay@isae.fr).

A. Hémercyck is with LAAS/CNRS, F-31031 Toulouse, France (e-mail: anne.hemeryck@laas.fr).

N. Richard, M. Raine, P. Paillet, and M. Gaillardin are with CEA, DAM, DIF, F-91297 Arpajon, France (e-mail: nicolas.richard@cea.fr).

L. Martin-Samos is with the Materials Research Laboratory, University of Nova Gorica, SI-5270 Ajdovščina, Slovenia (e-mail: layla.colomer@ung.si).

N. Mousseau is with the Université de Montréal, Department of Physics, Montréal, QC H3C 3J7, Canada (e-mail: normand.mousseau@umontreal.ca). Color versions of one or more of the figures in this paper are available online at <http://ieeexplore.ieee.org>.

Digital Object Identifier 10.1109/TNS.2018.2790843

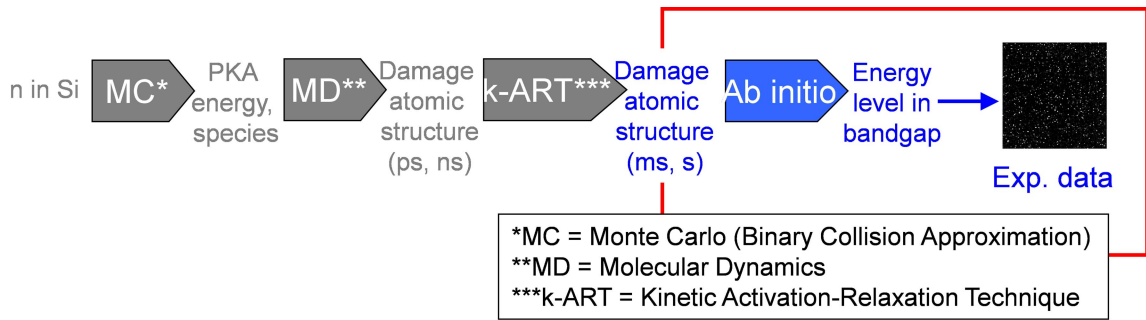


Fig. 1. Schematic of the global simulation project. The steps inside the scope of this paper are identified by red squares. The Part I and Part II correspond to [1] and [2]. Methods used are into the blue arrows. MC: Monte Carlo. MD: molecular dynamics. k-ART: kinetic activation relaxation technique.

DC measurements in irradiated devices have shown an evolution of the defected structures over different timescales ranging from a few seconds to several days [4], [5]. However, simulations performed in [2] have shown that the main changes in the defect structure all occur during a timescale lower than 1 s. After this period, the transformations of defect clusters are mainly due to the migration of bigger defect centers as 4V or 4I that may eventually recombine. These migrations take a long time and are only observable after long annealing times (days and more). As they can lead to the annealing of big defects, they can be responsible for the large reduction of DC experimentally observed in longer timescale.

This paper carries on this approach by characterizing the damaged structures obtained at the end of the k-ART step using FP calculations (the final step identified in red line in Fig. 1). In particular, we focus here on two “simple” defects centers, i.e., the divacancy (2V) and the tri-interstitial (3I). Their properties are analyzed and compared with DC and DC-RTS measurements on CMOS image sensors (CISs) [6], [7] and deep-level transient spectroscopy (DLTS) [8].

DC measurements performed on CIS have been chosen as the reference experimental data for several reasons. First, the sensitive depletion region of CIS pixels can be free of active Shockley–Read–Hall (SRH) generation center, leading to leakage current values as low as  $1 e^-/s$  at room temperature. In such a device, the creation of a single SRH generation center in the whole pixel array can thus be detected. Moreover, CIS allows the sampling of silicon with a large number of depleted microvolumes (as small as a few  $\mu m^3$ ) leading to a very accurate statistical analysis of DD in silicon. The CIS parameter that is the most sensitive to the presence of defects is the DC. For a given microvolume (i.e., a given pixel), this current is directly proportional to the number of defects and to the generation rate of the electron–hole pairs. Hence, a simple DC measurement on a CIS can provide a lot of valuable information about the defect distribution and configuration all over the silicon die.

In this paper, the details of the FP calculations are first described. The results concerning the defect properties at the atomic scale are then presented for the divacancy and the tri-interstitial, mostly regarding their configuration lifetimes and electronic levels in the gap. These results are then discussed and correlated with the macroscopic DC and DC-RTS phenomena observed in image sensors.

## II. CALCULATION DETAILS

FP calculations are used to obtain the total energy and electronic properties of each simple defect configuration extracted from the k-ART simulations. To do so, these configurations are embedded within a perfect diamond-like crystalline cell of about 216 atoms (i.e., 216 atoms corresponding to  $3 \times 3 \times 3$  elementary cells) for the perfect crystalline diamond Si cell without defects, 215 atoms for a monovacancy and 217 atoms for a monointerstitial, 214 atoms for a divacancy, and so on. This procedure leads to computationally affordable cell sizes for FP calculations and to a large distance, of about 30 Å, between the cluster defect and its periodic images. The electronic levels induced by several defects together in a bigger cell are nowadays impossible to evaluate due to computational cost drastically increasing with the number of atoms.

To relax the structures obtained from k-ART [2], density function theory (DFT) calculations in the local density approximation have been performed with the PWscf code from the quantum ESPRESSO distribution [9]. Norm-conserving pseudopotentials are applied to describe electron–ion interactions. The plane wave cutoff energy is fixed at 60 Ry and, thanks to the use of large supercells, the Brillouin zone needs to be sampled only at the  $\Gamma$  point. The cell parameters of each simulation cell is kept constant, equal to the ones of the perfect crystalline cell with its 216 atoms, and only the atomic positions have been allowed relaxing in order to obtain interatomic forces lower than  $10^{-3}$  Ry/a.u.

The obtained atomic positions and their corresponding wave functions are then used in one shot GW (i.e.,  $G_0W_0$ ) calculations performed with the SaX package version 2 [10]. This allows obtaining highly accurate density of states (DOSs) and electronic defect level positions (see [11], [12]). The need to go beyond DFT, using the GW approximation, is motivated by the known underestimation of the bandgap in semiconductor and insulating materials [13] and by the unpredictable error on the value of defect ionization potentials and electron affinities due to the local (or semilocal) nature of exchange–correlation functionals in DFT.

Details of the  $G_0W_0$  calculations are the following: we adopted 20-Ry energy cutoff for the Fock operator, 20-Ry energy cutoff for the irreducible polarizability, and the screened Coulomb potential. We included 1100 bands for the transition many-fold sampling, in the calculation of the GW Green functions. The Godby–Needs plasmon-pole

model [14] was used to model the energy dependence of the dielectric matrix. To obtain the energy states, only the vertical ionization potential and vertical electron affinities have been used, i.e., without the atomic relaxation due to the new charge state. The obtained accuracy on the energies states in the bandgap is of about 0.10 eV.

An important characteristic of an electronic state is its degree of localization. It is quantified by means of a normalized self-interaction ( $|SI|$ ), as discussed in [15]: the higher the value of SI, the stronger the localization. For  $|SI| = 1$ , the electronic state is as delocalized as a plane wave.

Migration pathways are used to calculate the average configuration lifetimes ( $\langle \tau \rangle$ ) of each defect structure using transition state theory that involves the knowledge of the surrounding saddle point that has the lowest energy barrier of migration  $E_b$

$$\langle \tau^{-1} \rangle = \frac{\prod_{\min} \omega_i}{\prod_{\text{saddle}} \omega_j} e^{-\frac{E_b}{k_B T}} \quad (1)$$

where the product over all the phonon frequencies  $\omega$  on the studied structure  $\prod_{\min} \omega_i$  is done over  $3N$  frequencies and  $3N - 1$  on the saddle point,  $N$  is the number of atoms,  $k_B$  is Boltzmann's constant, and  $T$  is the temperature. The ratio of the phonon frequencies is taken to be  $10^{-13}$  H as in most crystalline solids. This configuration lifetime is related to the probability of a structural change, i.e., the jump probability from a local minimum to another and, therefore, must not be confused with the recombination and generation lifetime of charge carriers.

For the calculation of migration pathways along the minimum energy path (MEP), the climbing-image nudged elastic band (NEB) is used to evaluate the energy barriers [16]. We used 13 intermediate images to describe the path with a high enough resolution in order to avoid missing an intermediate saddle point.

For a structure that has  $N$  possible configurations with respective energies  $E_{di}$  ( $i = 1, \dots, N$ ), the probability  $P_i$  that the system is in the configuration  $i$  is a function of  $E_{di}$  and of the partition of configurations  $Z$  defined as  $Z = \sum_n^N e^{-E_{dn}/(k_B T)}$

$$P_i = \frac{e^{-\frac{E_{di}}{k_B T}}}{Z}. \quad (2)$$

To calculate the average intensity ( $I_{dc}$ ) of the DC generated by one single state in the gap of a defect with an energy  $E_{\text{defect}}$ , the Sah–Noyce–Shockley theory is used

$$\langle I_{dc} \rangle \propto A e^{-\frac{E_a}{k_B T}} \quad (3)$$

where the prefactor  $A$  is a function of hole and electron capture cross sections, their thermal velocity, and their population. The prefactor  $A$  is proportional to  $T^2$  and estimated to be  $\ln(A) \approx 36$  at 300 K in our studied case, from the experimental value of the divacancy given in [6], [7], and [17]. The term  $E_a$  is commonly named the activation energy needed for one electron to go from the valence band to the conduction band.

The estimation of this activation energy depends on the number of electronic states in the bandgap, defined here as the vertical ionization potentials calculated within the GW approximation. A state in the bandgap becomes a bridge for

the electrons to travel from the valence band to the conduction band. When only one state with the associated energy  $E_t$  exits in the bandgap, the activation energy  $E_a$  needed to thermally activate the electrons is

$$E_a = \max(E_t - E_v; E_c - E_t) \quad (4)$$

where  $E_v$  and  $E_c$  are the energies corresponding to the top of the valence band and the bottom of the conduction band, respectively. However, when several states (for instance,  $E_{t1}$  and  $E_{t2}$ ) are into the gap, the electrons can sometimes use a multiple-step bridge such as  $E_v \rightarrow E_{t1} \rightarrow E_{t2} \rightarrow E_c$ . This multiple bridge pathway can occur only if the wave functions  $|\phi_{t1}\rangle$  and  $|\phi_{t2}\rangle$  of the two states  $t1$  and  $t2$  overlap. The activation energy is then

$$E_a = \min[\max_j(E_{j+1} - E_j); \max_i(E_i - E_v; E_c - E_i)] \quad (5)$$

where  $i$  covers all the nonoverlapping states and  $j$  covers all the overlapping states. The DC intensity is then calculated as in [8].

As rough estimate of the overlap between electronic states, we use the integral between their respective charge density. In this paper, it has been evaluated visually by plotting the isovalue of the charge density for each state at 50% of its maximum with the XCrySDden package. In our chosen case, this visual estimation is possible because the two wave functions are easily distinguishable: they are located either each in a different part of the space when their overlap is negligible, or both in the same part of the space when their overlap is important.

The formation energy  $E_f$  of a defect is the energy that the system has to give to create a defect. It is defined with respect to the total energy  $E_{216}$  of the pure silicon supercell as a function of the number of atoms  $n_a$  that the supercell contains and  $E_d$  the energy of the defective supercell as

$$E_f = - \left[ E_{216} \left( \frac{n_a}{216} \right) - E_d \right]. \quad (6)$$

### III. RESULTS

#### A. General Trends

As explained in [2], silicon PKA in bulk silicon at 300 K generate displacement cascades which finally result in amorphous clusters that are mainly composed of small simple defects centers, namely, 2V, 3V, 4V and 3I 4I. The fundamental understanding of the dynamic behavior and electronic properties of these resulting defect centers can provide a good insight on the macroscopic observations of DC and DC-RTS without studying the entire cluster.

Among all the defect centers, we choose to focus on the most meaningful two, which are playing an important role in the response of silicon to DD: the divacancy (2V) and the tri-interstitial (3I) defects. The two of them well depict the typical behaviors of DC-RTS and DC signals, respectively. In fact, they both have different configurations with lifetimes that vary from microsecond to years and also possess zero to three electronic levels in the bandgap, with and without intercenter charge transfer (ICCT) [8]. A full review paper

gathering the details of all simple defects in bulk silicon will be published in a near future.

To understand the origin of the DC and DC-RTS using FP calculations, we focus our study on the possible configurations of each defect, the corresponding migration barrier to travel between such configurations, their lifetimes, and the corresponding electronic levels that appear in the bandgap.

For a given defect, the configuration with the lowest formation energy (the ground state) is the most stable and consequently is the one that is mainly observed experimentally. But several other stable or metastable states can also exist, that can differ from the ground state by small structural changes (interatomic distances) or can be topologically different in terms of close neighborhood.

The diffusion barrier gives information about the possibility to observe the defects experimentally. Indeed, defects that can diffuse at the experimental temperature are not observed because they tend to agglomerate to form bigger defect clusters, and/or they are trapped at the interfaces. Notably, among all the simple defects, the 1V, 1I, and 2I possess energy barriers that are small enough to diffuse at 300 K (0.23, 0.30, and 0.15 eV, respectively, in our *ab initio* calculations for the neutral state), whereas the 2V, 3V, 4V and 3I, 4I exhibit migration barriers larger than 0.50 eV, which are large enough to keep these defects into the silicon bulk at room temperature. The diffusion barrier is thus calculated for each defect. Note that the diffusion coefficient depends on the temperature so that the observation time is strongly correlated with the operation temperature.

The lifetime associated with each configuration of a defect gives information about the kind of DC generation that is created by the defect, i.e., DC-RTS or constant DC. This depends on the experimental integration time, i.e., the duration of the accumulation of electrons before counting them, and acquisition time (duration of the total measurement). A defect generates a constant DC in two cases. First, if the lifetimes of its configurations are lower than those of the integration time: several changes in configurations can occur during the integration time and only an average of all the generations' rates is counted, generating a constant DC. Second, a defect also generates a constant DC if the lifetimes of its configurations are higher than those of the acquisition time: no change of configuration occurs during the experiment. A defect generates DC-RTS if the lifetimes of its configurations are higher than those of the integration time and lower than those of the acquisition time: the DC signal is constant during several periods of integrations and strongly varies when the configuration changes. The average lifetime is a constant for a given temperature, but the kind of generation rate that is observed depends on the experimental conditions. As all the defects exist in several stable and metastable atomic configurations, they are all able to generate different kinds of DC only measurable by changing both the integration and acquisition times.

Note that for the same defect, lifetimes can be very different. Indeed, two main trends are observed in the energy barriers required to switch from one configuration to another for the same defect. On the one hand, the configurations that are

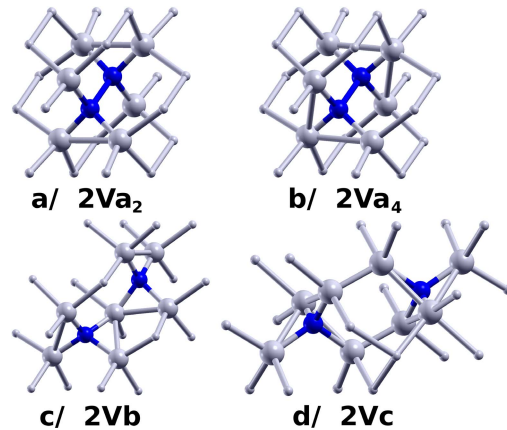


Fig. 2. Different configurations of the divacancy obtained after k-ART simulations of 1 s, and relaxed and characterized using FP calculations. (a) 2Va<sub>2</sub>. (b) 2Va<sub>4</sub>. (c) 2Vb. (d) 2Vc. Gray balls: Silicon atoms. Big gray balls: first neighbor silicon atoms of a vacancy. Blue balls: crystalline sites without any atoms, i.e., vacancies.

topologically different are separated by energy barriers higher than  $\sim 0.40$  eV. On the other hand, the configurations that differ only by a change in their atomic distances and conserve their neighboring topology are separated by lower energy barriers.

The energy levels are the last information that is used in our study. They give information of the intensity of the generated DC. Concerning the electronic states, the same trends are observed. Configurations with the same topology exhibit very similar DOS, whereas configurations with different topologies have different DOSs. The number of states in the bandgap is difficult to predict and varies between zero and four in the studied defects 2V and 3I.

### B. Divacancy Defect

The divacancy has been widely detected in CMOS after irradiation [7] and plays a crucial role as a DC generation center. In our calculations, the divacancy appears after one second of annealing, and we observe that it possesses a high number of metastable configurations. The most stable ones are shown in Fig. 2 and are classified from the lowest to the highest total energy: two vacancies as the first neighbor (2Va), as the second neighbor (2Vb), and as the third neighbor (2Vc). For the 2Va configuration, two configurations exist, named, 2Va<sub>2</sub> and 2Va<sub>4</sub> [Fig. 2(a) and (b)], 2Va<sub>2</sub> being the most stable one. Contrary to the 2Va, 2Vb, and 2Vc configurations that have different topologies, 2Va<sub>2</sub> and 2Va<sub>4</sub> are only distinguishable by their different interatomic distances. In fact, due to the local reconstruction, a weak electronic bond is also sometimes formed between two Si atoms when the interatomic distance is lower than 3 Å.

The MEP for the diffusion of the divacancy from its ground state 2Va<sub>2</sub> to a neighbor 2Va<sub>2</sub> occurs through the 2Vb or 2Vc configuration. This diffusion needs the crossing of a 1.11-eV energy barrier, as shown in Fig. 3 for Va<sub>2</sub>, coherent with experimental observations [18]. This high barrier implies that no diffusion of the divacancy can be observed at 300 K. The 2Vb configuration is a highly metastable state that rapidly

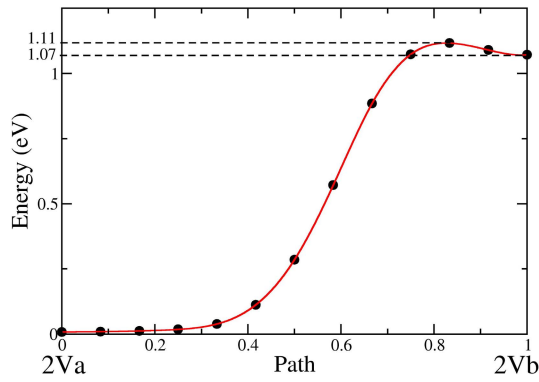


Fig. 3. Migration path between the  $2Va_2$  and the  $2Vb$  configurations. The energy barrier  $2Va_2 \rightarrow 2Vb_2$  is 1.11 eV, whereas the energy barrier  $2Vb \rightarrow 2Va_2$  is 0.04 eV.

TABLE I

DIFFUSION BARRIER IN ELECTRONVOLT FROM ONE TO ANOTHER 2V CONFIGURATION (TOP). FOR EACH 2V CONFIGURATION: THE FORMATION ENERGY  $E_f$  IN eV/at., THE TOTAL ENERGY WITH RESPECT TO THE GROUND STATE  $2Va_2 \Delta Z$ , THE AVERAGE LIFETIME ( $\tau$ ) AT 300 K IN SECOND, AND THE OCCUPATION PROBABILITY  $P$  (BOTTOM)

From/to	$2Va_2$	$2Va_4$	$2Vb$	$2Vc$
$2Va_2$	-	0.004	0.04	0.61
$2Va_4$	0.004	-	0.04	0.61
$2Vb$	1.11	1.11	-	0.06
$2Vc$	1.92	1.92	0.36	-
	$2Va_2$	$2Va_4$	$2Vb$	$2Vc$
$E_f$	4.92	4.92	5.99	6.28
$\Delta E$	0	0	1.07	1.36
$\langle \tau \rangle$	$10^{-13}$	$10^{-13}$	$10^{-13}$	$10^{-12}$
$P$	0.50	0.50	$10^{-19}$	$10^{-24}$

tends to stabilize in the ground state  $2Va_2$ . The resulting lifetimes, the occupation probabilities, and the diffusion barriers for the 2V configurations are summarized in Table I.

The occupation probabilities of the  $2Vb$  and  $2Vc$  configurations are very small, so that they would not be observed experimentally. Nevertheless,  $2Vb$  and  $2Vc$  are metastable “transition” states that are reached during the diffusion process of the divacancy.

On the contrary, the two  $2Va$  configurations are the ones with the largest occupation probabilities. Because of their equal formation energies, these two probabilities are equivalent. However, the lifetimes of these two  $2Va$  configurations are very small (less than 1  $\mu s$ ) because of the small energy barrier (0.004 eV) that separates them, so that these two structures pass from one state to the other billion times per seconds at 300 K. The  $2Va$  system is thus trapped in a quasi-permanent oscillation between the two configurations  $2Va_2$  and  $2Va_4$ , whereas the high-energy barriers (1.11 eV) required to separate the two vacancies cannot be overcome at 300 K.

The electronic DOS is given in Fig. 4 for the  $2Va_2$  and  $2Va_4$  configurations in GW approximations. The GW approximation gives a bandgap of 1.06 eV, with only 5% of error compared to experimental one (1.12 eV [19]). This error was 50% for DFT (not shown here).

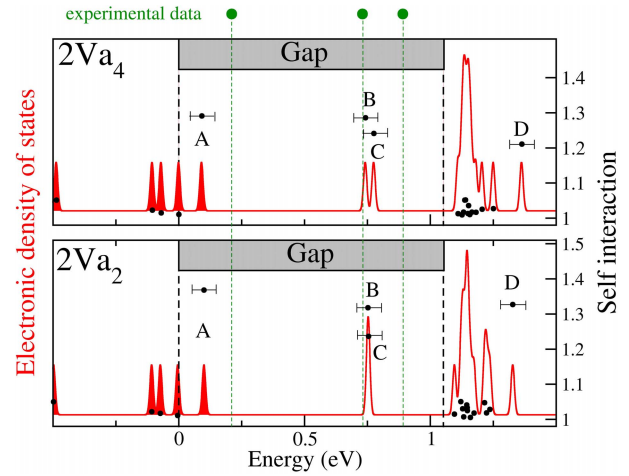


Fig. 4. DOS calculated within the GW approximation for the most observed configurations of divacancy defect: the  $2Va_4$  (top) and  $2Va_2$  (bottom). Letters are here to mark the defect energy levels. The states occupied at 0 K are filled. The experimental data from [19] and [20] are in green. The horizontal line represents the accuracy.

TABLE II

FOR EACH CONFIGURATION OF THE DIVACANCY DEFECT, ENERGY LEVELS INTRODUCED IN THE BANDGAP (ELECTRONVOLT) WITH RESPECT TO THE VALENCE BAND, ACTIVATION ENERGY  $E_a$  IN ELECTRONVOLT, AND ITS GENERATION RATES  $R$  IN  $e^-/s$  BY USING  $\ln(A) = 36$ . EMPTY STATES ARE IN BOLD

Conf.	Energy levels	$E_a$	$R$
$2Va_2$	0.10; <b>0.75; 0.75</b>	0.65	150
$2Va_4$	0.09; <b>0.74; 0.77</b>	0.64	141
$2Vb$	<b>0.91; 1.01</b>	0.91	2
$2Vc$	<b>0.80; 0.84</b>	0.80	4

Three electronic levels have been observed experimentally, supposed to be in one of the most probable configurations ( $2Va_2$  or  $2Va_4$ ).

By *Electronic Paramagnetic Resonance*:

$$E_c - 0.23 \text{ eV (charged-)} [19].$$

By *Infrared Spectroscopy*:

$$E_c - 0.39 \text{ eV (charged 0)} [19].$$

By *Dlts*:

$$E_v + 0.21 \text{ eV (charged+)} [19], [20]$$

where  $E_v$  and  $E_c$  are the top of the valence band and the bottom of the conduction band, respectively. Vadja and Cheng [19] and Bourgoïn and Lannoo [20] explain that  $E_v + 0.21$  eV is a hole acceptor state, whereas  $E_c - 0.23$  eV and  $E_c - 0.39$  eV are electrons acceptors states. In our results given in Table II, for the  $2Va_4$  configuration, we find the hole acceptor at  $E_v + 0.09$  eV, and the two electron acceptor states are located at  $E_v + 0.74$  eV, equal to  $E_c - 0.32$  eV by using our 1.06-eV bandgap, and  $E_v + 0.77$  eV equal to  $E_c - 0.29$  eV. These values are in good agreement with the experimental values, taking into account the accuracy of the GW calculations (0.10 eV).

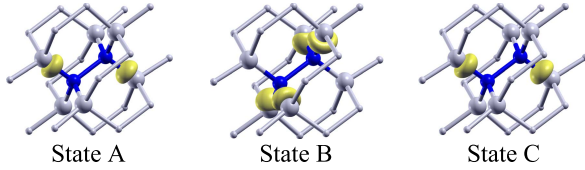


Fig. 5. Electronic wave function square of the three electronic states A, B, and C in the bandgap of bulk silicon due to  $2V_{a2}$  configuration presented in Fig. 2(a). Blue balls: vacancy sites. Big gray balls: Silicon atoms that are the first neighbors of the vacancies. Small gray balls: other silicon atoms on crystalline sites. The yellow surface represents that the isovalue for a probability to find the electron equals 50%. The electron is mainly located inside the volume delimited by this yellow surface.

The  $|SI|$  previously defined allows us to distinguish the states induced by the defect. As shown in Fig. 4, the  $2V_{a2}$  configuration generates four main states, namely, A, B, C, and D. Among them, only the states A, B, and C are into the bandgap and only the state A is filled at 0 K, in good agreement with experimental observations [19], [20]. All these states can serve as “bridges” for the electrons to travel from the valence band to the conduction band. To evaluate the activation energy of this defect using (5), one should first evaluate the overlapping integral between these defect states. For the three states A, B, and C in the bandgap, the presence probability, square of the electronic wave functions, is drawn in Fig. 5. Since atoms are missing, the electrons involved in these states do not form bonding orbitals (Fig. 5). Fig. 5 shows that neither overlapping occurs between states A and B nor between states B and C because the electrons are located on different atoms. On the contrary, a drastic overlapping occurs between states A and C, because they both form a dangling bond on the same atom and in the same direction. In the specific case of  $2V_{a2}$ , the calculated activation energy is then determined as the highest barrier of the easiest path for the electrons to go from valence to conduction band, i.e., the one that required the less energy.

This path is  $E_{val} - E_A - E_C - E_{cond}$ , and its highest barrier is between the energy levels of the two states A and C:  $|0.75 - 0.10| = 0.65$  eV. This is the first theoretical confirmation that the hypothesis proposed by Watts [8] of charge transfer between several electronic levels occur. Moreover, the activation energy that we obtained here (i.e., 0.65 eV) has also been measured in the literature (0.64 eV in averages) using the Arrhenius law in CMOS [7] or the generation rate and DLTS in diodes [8] (a full review is given in [4] for 2V and other defects). Therefore, the measured activation energy of 0.64 eV could be ascribed to the switching between  $2V_{a4}$  and  $2V_{a2}$  configurations.

For all 2V configurations, the energy levels into the bandgap are summarized in Table II, with the corresponding estimated generation rate. As the two  $2V_a$  configurations have the same topology and differ only by their interatomic distances, their respective DOS is quite similar: they both have three defect states in the gap for which the energy difference is smaller than 0.02 eV. However, this small difference is high enough to slightly change the activation energy and then highly change the generation rate of each configuration.

In the case of the  $2V_b$  and  $2V_c$  configurations, different DOSs are obtained, with a different number of states due to

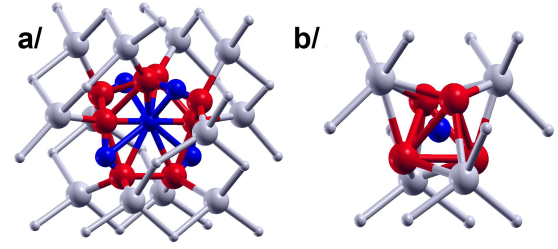


Fig. 6. Two configurations of the tri-interstitial [(a)  $3I_{block}$  and (b)  $3I_{tetra}$ ] obtained after k-ART simulations and relaxed and characterized using FP calculations. Gray balls: Silicon atoms. Big gray balls: Silicon atoms in the first neighbor of a vacancy. Blue balls: crystalline sites without any atoms, i.e., vacancies. Red ball: interstitial silicon atoms.

TABLE III

FOR EACH CONFIGURATION OF THE TRI-INTERSTITIAL, ITS FORMATION ENERGY  $E_f$  (eV/at.), ITS ENERGY WITH RESPECT TO THE GROUND STATE ( $\Delta E$ ), ITS AVERAGE LIFETIME ( $\tau$ ) AT 300 K (SECOND), ITS OCCUPATION PROBABILITY  $P$  AMONG ALL THE CONFIGURATIONS (PERCENTAGE), AND ITS MINIMUM ENERGY NEEDED TO GO FROM ONE CONFIGURATION TO ANOTHER. ALL THE VALUES ARE IN ELECTRONVOLT

From/to	$3I_{tetra}$	$3I_{block}$
$3I_{tetra}$	-	2.60
$3I_{block}$	2.62	-
$E_f$	5.39	5.41
$\Delta E$	0	0.02
$\langle \tau \rangle$	$10^{31}$	$10^{31}$
$P$	0.68	0.32

their different topologies. The overlapping integral between the states of the  $2V_b$  and  $2V_c$  structures is null, so that (4) is used to evaluate the activation energy.

### C. Tri-Interstitial Defect

The same approach is conducted for the tri-interstitial defect.

The tri-interstitial exists in several configurations. The two most stable ones are the  $3I_{block}$  and the  $3I_{tetra}$  [21], both represented in Fig. 6. All the other configurations have a much higher energy or correspond to the di-interstitial surrounded by another interstitial.

The MEP for the diffusion of the tri-interstitial from its ground state  $3V_{tetra}$  to a neighbor  $3V_{tetra}$  needs the crossing of a 0.45-eV barrier coherent with previous work (0.49 eV [22]) [21], whereas this barrier is 2.59 eV for the diffusion from a  $3V_{block}$  configuration to a  $3V_{block}$  configuration. For this reason, during annealing, all the  $3V_{tetra}$  configurations diffuse, whereas the  $3V_{block}$  does not.

Their average lifetime and occupation probability are given in Table III. These two structures have quite the same formation energy ( $\Delta E = 0.02$  eV), so that their occupation probabilities are of the same order of magnitude. The energy barrier that separates them is very large ( $>2$  eV), which means that a configuration change from one to another cannot be observed experimentally during reasonable times.

The energy levels and generation rates of the two configurations are given in Table IV. The configuration  $3I_{block}$  does not create energy levels in the bandgap. Hence, its generation rate  $R$  is null at 300 K because the all gap has to be crossed.

TABLE IV

FOR EACH CONFIGURATION OF THE TRI-INTERSTITIAL DEFECT, ENERGY LEVELS INTRODUCED IN THE GAP (ELECTRONVOLT) WITH RESPECT TO THE VALENCE BAND, ACTIVATION ENERGY  $E_a$  (ELECTRONVOLT), AND ITS GENERATION RATES  $R$  ( $e^-/s$ ) BY TAKING  $\ln(A) = 36$

Conf.	Energy levels	$E_a$	$R$
$3I_{\text{block}}$	-	1.06	0
$3I_{\text{tetra}}$	0.92	0.92	2

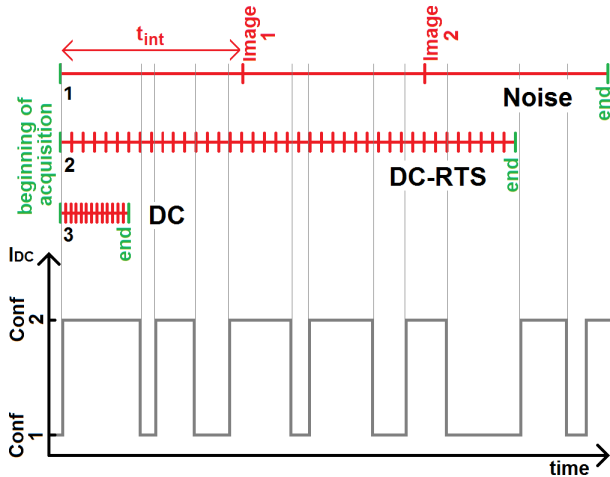


Fig. 7. For the same defect with two configurations, three different experiments with different integration and acquisition times that generate a noise, a DC-RTS, or a DC. Gray line: intensity of the DC as a function of the time. Green bars: beginning and end of an acquisition. Red bars: end of the integration time for the collection of the electrons, i.e., generation of an image.

On the contrary, the configuration  $3I_{\text{tetra}}$  has a generation rate, which means that those two structures can easily be distinguished using  $E_a$  or  $R$ .

#### IV. DISCUSSION

In this section, we use the FP results for the divacancy and tri-interstitial defects to investigate if their presence in a CIS generates or not a DC, and if this DC is a DC-RTS or only an average DC (noise). The kind of measured signal depends on the number of configurational transitions that occur during the integration time and the total acquisition time. The total acquisition time is the duration of the experiment, whereas the integration time is the duration for which electrons are collected between two images. Three kinds of DC can be observed. First, if several transitions occur during one integration time (Fig. 7, example 1), the observed intensity is the average value of the generation rate of each configuration weighted by their occupancy. The resulting signal is an apparent stable DC with a small noise between two images due to the random change of configuration that slightly change the average DC (Fig. 7, example 1). Second, if several transitions occur during the total acquisition time but not during the integration time (Fig. 7, example 2), the observed signal exhibits a clear RTS behavior. Third, if no transition occurs during the total acquisition time, a constant DC is observed (Fig. 7, example 3).

For a standard observation at 300 K, acquisition times can be as long as a day, and integration time as long as a second. Hence, even if both 3I and 2V defects exist in several configurations and exhibit electronic levels into the bandgap, they do not generate the same DC because they have different configuration lifetimes.

In the case of the 3I, each configuration is trapped in a deep potential energy well, which gives it a great stability. Their resulting lifetimes at 300 K are higher than one year so that a configuration can hardly change during an observation. Moreover, the  $3I_{\text{block}}$  configuration does not have any states in its bandgap (Table III) and is then not a generation center: no DC is observed in this configuration. On the contrary, the  $3I_{\text{tetra}}$  configuration has one state into its bandgap and is a generation center: its resulting signal is then a simple DC (Fig. 7, example 3).

In the case of the 2V, the integration time is generally larger than the configuration lifetime, so that a large number of transitions between  $2Va_2$  and  $2Va_4$  occurs during a given integration time. During an acquisition, the observed generation rate is then an average of the one of each configuration. The DC is then a noise that varies around this average value (Fig. 7, example 1).

Nevertheless, for a multiconfiguration defect, the three kinds of current (noise, DC-RTS, and DC) could possibly be observed. This can be done by changing the integration time, or the acquisition time or the temperature, which is correlated to the configuration lifetimes. For example, a DC-RTS could possibly be observed for the 3I by increasing the temperature, and for 2V, by decreasing drastically the temperature. However, signal magnitude varies exponentially with temperature, and even if the RTS time constants of 3I and 2V could fall into the experimental windows, it is not likely that the generated amplitude will be observable (or that the image sensor can be operated at the optimum temperature).

The large number of different DC intensities that are observed in irradiated CMOS compare to the small number of different defects (2V, 3V, 4V, 3I, 4I) that compose the clusters at the end of the annealing is due to their proximity in terms of distance. In fact, the energy levels that are evaluated in Section III can slightly vary if other defects are around and generate elastic distortions that change the interatomic distances. For this reason, the intensity of the DC generated by a cluster of defect is hardly predictable without the entire knowledge of its structure.

#### V. CONCLUSION

In order to describe the DD in silicon, we carry on our original simulation approach by characterizing the defect structures coming from k-ART calculations using FP calculations. Here, we focus on the divacancy and tri-interstitial defects. We evaluate their atomic structures, and we calculate their formation energy, their occupation probability, and their configuration lifetimes using NEB. By using GW to calculate their DOS, we show that the states created by each configuration of the same defect in the bandgap of silicon can lead to different DC values. These configurations with different properties can lead to DC or DC-RTS as a function of

experimental integration time. This paper demonstrates the ability of our simulation approach to obtain results that can be discussed and compared to experimental characterizations. In particular, for the divacancy, the experimental electronic levels from [19] and [20] have been well reproduced using the GW approximation, and then, the ICCT that was supposed in [8] to justify the measurement of a too low activation energy has been clearly confirmed in our simulations using the overlapping between wave functions of two electronic states. The small quantitative discrepancies found between our modeling results and the experimental observations are within the overall computational precision of 0.10 eV (within 9% of the silicon gap).

As a perspective, the role of dopants and impurities could be investigated as both may open additional current channels. Moreover, the question whether or not the electric field (operating condition of CMOS) could affect the different calculated properties is still an open question. The charge state of the defect can also change its energy levels and/or migration barriers. Other key parameters used in the SRH theory that have not been calculated yet are the electron and hole cross sections. Both vary by several orders of magnitude ( $10^{-13}$ – $10^{-16}$  cm<sup>2</sup> [4]) for a given defect, highly changing the resulting generation rate. Moreover, measured energy levels and cross sections are different for the recombination rate observed in silicon-based solar cells or bipolar transistors. In addition, even if the probability of having ICCT can be linked to the number of defects centers in the cluster (see [2], [7]), it is still unclear how to account quantitatively for the measured current. These questions will be the subject of future studies, as well as extending the calculations to other defects (1V, 3V, 4V and 1I, 2I, 4I).

#### ACKNOWLEDGMENT

The authors would like to thank S. Girard, J. M. Belloir, C. Virmondois, and C. Durnez for their fruitful discussions.

#### REFERENCES

- [1] M. Raine *et al.*, “Simulation of single particle displacement damage in silicon—Part I: Global approach and primary interaction simulation,” *IEEE Trans. Nucl. Sci.*, vol. 64, no. 1, pp. 133–140, Jan. 2017.
- [2] A. Jay *et al.*, “Simulation of single particle displacement damage in silicon—Part II: Generation and long-time relaxation of damage structure,” *IEEE Trans. Nucl. Sci.*, vol. 64, no. 1, pp. 141–148, Jan. 2017.
- [3] J. R. Srour and J. W. Palko, “Displacement damage effects in irradiated semiconductor devices,” *IEEE Trans. Nucl. Sci.*, vol. 60, no. 3, pp. 1740–1766, Jun. 2013.
- [4] J. R. Srour, C. J. Marshall, and P. W. Marshall, “Review of displacement damage effects in silicon devices,” *IEEE Trans. Nucl. Sci.*, vol. 50, no. 3, pp. 653–670, Jun. 2003.
- [5] B. L. Gregory and H. H. Sander, “Transient annealing of defects in irradiated silicon devices,” *Proc. IEEE*, vol. 58, no. 9, pp. 1328–1341, Sep. 1970.
- [6] J. M. Belloir *et al.*, “Dark current spectroscopy in neutron, proton and ion irradiated CMOS image sensors: From point defects to clusters,” *IEEE Trans. Nucl. Sci.*, vol. 64, no. 1, pp. 27–37, Jan. 2017.
- [7] J.-M. Belloir *et al.*, “Dark current spectroscopy on alpha irradiated pinned photodiode CMOS image sensors,” *IEEE Trans. Nucl. Sci.*, vol. 63, no. 4, pp. 2183–2192, Aug. 2016.
- [8] S. J. Watts, J. Matheson, I. H. Hopkins-Bond, A. Holmes-Siedle, A. Mohammadzadeh, and R. Pace, “A new model for generation-recombination in silicon depletion regions after neutron irradiation,” *IEEE Trans. Nucl. Sci.*, vol. 43, no. 6, pp. 2587–2594, Dec. 1996.
- [9] P. Giannozzi, “QUANTUM ESPRESSO: A modular and open-source software project for quantum simulations of materials,” *J. Phys., Condens. Matter*, vol. 21, no. 39, p. 395502, 2009.
- [10] L. Martin-Samos and G. Bussi, “SaX: An open source package for electronic-structure and optical-properties calculations in the GW approximation,” *Comput. Phys. Commun.*, vol. 180, no. 8, pp. 1416–1425, 2009.
- [11] N. Richard *et al.*, “Oxygen Deficient Centers in silica: Optical properties within many-body perturbation theory,” *J. Phys., Condens. Matter*, vol. 25, no. 33, p. 335502, 2013.
- [12] B. Winkler *et al.*, “Correlations between structural and optical properties of peroxy bridges from first principles,” *J. Phys. Chem. C*, vol. 212, no. 7, pp. 4002–4010, 2017.
- [13] M. van Schilfgaarde, T. Kotani, and S. Faleev, “Quasiparticle self-consistent GW theory,” *Phys. Rev. Lett.*, vol. 96, p. 226402, Jun. 2006.
- [14] R. W. Godby and R. J. Needs, “Metal-insulator transition in Kohn-Sham theory and quasiparticle theory,” *Phys. Rev. Lett.*, vol. 62, pp. 1169–1172, Mar. 1989.
- [15] L. Martin-Samos, G. Bussi, A. Ruini, E. Molinari, and M. J. Caldas, “Unraveling effects of disorder on the electronic structure of SiO<sub>2</sub> from first principles,” *Phys. Rev. B, Condens. Matter*, vol. 81, p. 081202, Feb. 2010.
- [16] G. Henkelman, B. P. Uberuaga, and H. Jonsson, “A climbing image nudged elastic band method for finding saddle points and minimum energy paths,” *J. Chem. Phys.*, vol. 113, no. 22, pp. 9901–9904, 2000.
- [17] C. Virmondois, “Analyse des effets des déplacements atomiques induits par l’environnement radiatif spatial sur la conception des imageurs CMOS,” Ph.D. dissertation, CNES, Toulouse, France, 2012.
- [18] L. C. Kimerling, P. Blood, and W. M. Gibson, *Radiation Effects in Semiconductors*, vol. 31, N. B. Urli and J. W. Corbett, Eds. Bristol, U.K.: Institute of Physics, 1977, p. 221.
- [19] P. Vadja and L. J. Cheng, “Low temperature photoconductivity in electron—Irradiated p-type Si,” *J. Appl. Phys.*, vol. 42, nos. 3–4, pp. 245–248, 2006.
- [20] J. Bourgoin and M. Lannoo, *Point Defects in Semiconductors II, Experimental Aspects*. New York, NY, USA: Springer-Verlag, 1983.
- [21] D. A. Richie, J. Kim, S. Barr, K. R. A. Hazzard, R. Hening, and W. J. Wilkins, “Complexity of small silicon self-interstitial defects,” *Phys. Rev. Lett.*, vol. 92, no. 4, p. 045501, 2004.
- [22] Y. A. Du, S. A. Barr, K. R. A. Hazzard, T. J. Lenosky, R. G. Hennig, and J. W. Wilkins, “Fast diffusion mechanism of silicon tri-interstitial defects,” *Phys. Rev. B*, vol. 72, p. 241306, Dec. 2005.
- [23] C. T. Sah, R. N. Noyce, and W. Shockley, “Carrier generation and recombination in p-n junctions and p-n junction characteristics,” *Proc. IRE*, vol. 45, no. 9, pp. 1228–1243, 1957.
- [24] L. K. Béland, P. Brommer, F. El-Mellouhi, J. F. Foly, and N. Mousseau, “Kinetic activation-relaxation technique,” *Phys. Rev. E, Stat. Phys. Plasmas Fluids Relat. Interdiscip. Top.*, vol. 84, p. 046704, Oct. 2011.